4. The methods of investigation: principles and experimental details

4.1. Thermal desorption spectroscopy (TDS)

4.1.1. Fundamental aspects

The thermal desorption spectroscopy (TDS), also named temperature programmed desorption (TPD), was introduced by I. Langmuir [La16] and is an extensively used – since experimentally relatively simple – technique in surface science and catalysis [Pe72, Ki75, Me82, Wo86, Kr91, Ch91]. TDS is often employed for determining coverages and for evaluating activation energies and frequency factors of desorption. After appropriate calibration, it is also possible to measure absolute coverages and sticking coefficients with high accuracy. Within the framework of suitable models, adsorbate-substrate binding energies and entropies can be calculated.

In a TDS experiment, we heat the adsorbate-covered sample with a defined heating rate, $\beta = dT/dt$, from a temperature below to a temperature above the expected desorption temperature of the adsorbate, and simultaneously detect the partial pressures, p_i, of the desorbing species with a mass spectrometer. In a pumped recipient, we obtain curves $p_i = p_i(t,T)$ with one or more maxima, the thermal desorption spectra.

A frequently used basis for the evaluation of kinetic parameters from thermal desorption spectra is the Polanyi-Wigner equation (Eq. 4.1) [Hi58]:

$$\text{desorption rate } R_{des} \equiv -\frac{d\Theta}{dt} = -\frac{d\Theta}{dT}\frac{dT}{dt} = -\frac{d\Theta}{dT}\beta = \nu_n\Theta^n \exp\left(-\frac{E_{des}}{RT}\right), \qquad \text{(Eq. 4.1)}$$

with the coverage Θ, the frequency factor ν_n, the desorption order n, and the desorption activation energy E_{des}. The other symbols have their usual meanings.

The 'parameters' E_{des}, n, and ν_n should generally be considered as functions of coverage and may in cases of complex kinetics (e.g., a phase equilibrium on the surface) also depend on the desorption temperature, which is a function of the heating rate (see below). That means, the desorption parameters can depend on the conditions of the TD experiment.

Within the general limitation of kinetic measurements, viz., proposed mechanisms can only be excluded, not be proven, TDS is also a method suitable for investigating desorption mechanisms. The desorption order, if interpreted as the molecularity of an elementary reaction, allows insight into the nature of the rate-limiting step of the desorption process, which is, from the kinetical point of view, in general a consecutive reaction. From the molecularity of the desorption process we can often draw conclusions about the state of the adsorbate itself. To give an example, a desorption order of two suggests a bimolecular bimolecular reaction as rate-limiting step, e.g., the combination of

two fragments. If the desorbing molecule is of the type X_2, than a species $X(ad)$ is likely to exist on the surface. In contrast, in the case of an adsorbate species $X_2(ad)$ we expect a first-order desorption kinetics. Fractional or strongly coverage-dependent orders suggest desorption from – or in the presence of – islands (see Chapter 6).

The measurement and interpretation of TD spectra relies on numerous implicit assumptions [Pe72, Me82]. They appear quite often to be fulfilled, one should, however, be aware of them. For example, the partial pressure of the desorbing species, p_i, measured by QMS, is only proportional to R_{des} if the pumping speed is infinitely large. This, however, is not really desirably since it leads to $p_i \rightarrow 0$. We circumvented this dilemma with our experimental setup and measured particle fluxes (vide infra), which inherently are proportional to R_{des}, instead of partial pressures.

4.1.2. Experimental aspects

DETECTION OF THE DESORBING SPECIES – The thermal desorption measurements were performed by means of a differentially pumped Balzers QMG 112 quadrupol mass spectrometer (QMS) mounted in a small separate chamber (V $\approx 1500 \text{ cm}^3$) connected with the main chamber by a small orifice ($\varnothing$ 2.8 mm). This orifice was moved close (< 0.1 mm) to the surface to suppress contributions from sample holder, crystal rim etc.
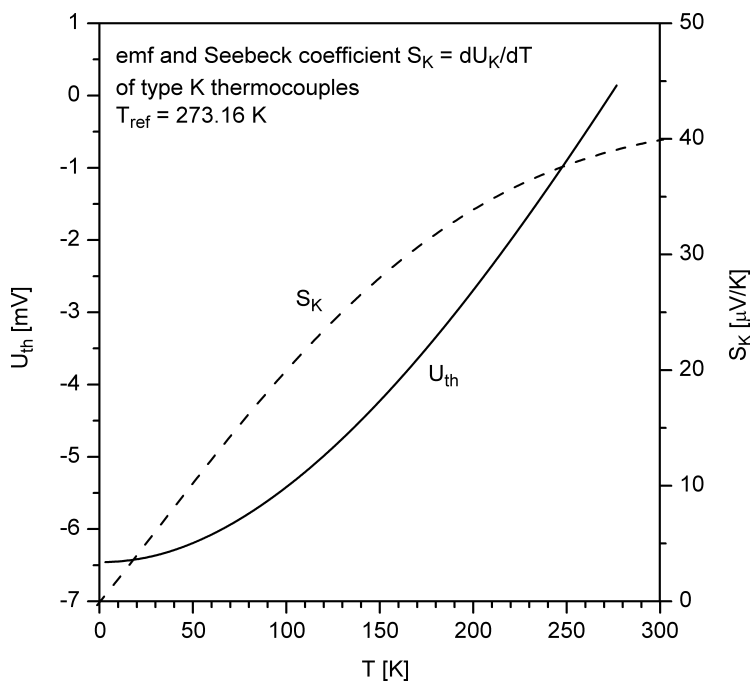

Fig. 4.1: Temperature measurement with type K thermocouples: thermovoltage U_{th} and Seebeck coefficient S_K in the low-temperature range. Reference temperature for U_{th} is 273.16 K.

TEMPERATURE MEASUREMENT – The sample temperature was monitored by means of a chromel-alumel (type K) thermocouple mounted directly on the crystal rim. The complete connections between sample and external preamplifier, including feedthroughs and connectors, were made from the same materials. The type K thermocouple can be used for the measurement of temperatures up to 1640 K. At 28 K, which is the lowest sample temperature accessible with our cooling system (see Section 4.6), the Seebeck coefficient, S_K, is reduced to ≈ 5 µV/K, compared to ≈ 40 µV/K at 298 K (see [Ne87] and Fig. 4.1). This change in S_K makes the *absolute* error ≈ 8 times larger at 28 K as compared to 298 K, and the *relative* error even ≈ 80 times larger. In order to keep the noise level in the temperature measurement low, which is important especially with respect to the temperature control during a TDS experiment, the input noise level of the thermovoltage amplifier has to be extremely small. Desirable was a noise of < 0.05 K at 28 K, which is equivalent to < 250 nV at the amplifier input. Furthermore, the amplifier should resist high voltage (2 kV) in order to allow 'indirect' sample heating by electron impact. These requirements were met by the thermovoltage-preamplifier HS210-K (amplification 150×), developed by H. Schlichting, with an noise level < 200 nV. It possesses an internal thermal reference point, kept at a constant temperature of 45°C. The zero point is electronically shifted to $T = 0$ K. A home-built ground-free isolation amplifier, equipped with a capacitive signal coupler, was switched between preamplifier and AD converter. For temperature control purposes, the amplified thermovoltage was fed into a PC via a 16-bit analog-digital converter (ADC) (Computer Boards, Inc.).

TEMPERATURE CONTROL – Only TD spectra taken with a constant heating rate, β, can be quantitatively analysed with the methods as described below, which makes a careful temperature control very important. Unfortunately, the Seebeck coefficient of the type K thermocouple changes strongly with T in the low-temperature (LT) range (see Fig. 4.1). Therefore, it is not useful to control the temperature in this range with the directly measurable thermovoltage, U_{th}, and a linear PID controller, because the change of S_K with T is equivalent to a change of the amplification factors in the proportional, α_P, integral, α_I, and differential part, α_D, of the PID control variable I_{out}:

$$I_{out} = I_{out,0} + \alpha_P\, \Delta U_{th} + \alpha_I \sum \Delta U_{th} + \alpha_D\, \Delta(\Delta U_{th}) \qquad\qquad \text{(Eq. 4.2)}$$

Herein, I_{out} denotes a variable proportional to the sample heating current, and $I_{out,0}$ is the initial value of I_{out}. ΔU_{th}, the control upset, is the difference between the actual and the desired thermovoltage (control input). In order to avoid these difficulties, we used the temperature difference itself to describe the control upset. For this purpose, U_{th} was digitized with a 16-bit ADC and, after averaging over 100 values, converted into

temperatures, T_A, by comparison with tabulated $T(U_{th})$ values. Then, the temperature difference, $\Delta T = T_A - T_T$, between the actual, T_A, and the desired temperature, T_T, was calculated. Now, the heating current, I_{out}, was determined by Eq. 4.2 with ΔU_{th} replaced by ΔT. The variable I_{out} controlled a digital-analog converter (DAC) (Computer Boards, Inc.), and the output voltage of the latter was used to control a commercial power supply unit (Systron Donner) for the (resistiv) sample heating. A further DAC was employed to control the quadrupol mass filter, and this allowed the detection of several masses at a certain temperature. With a proper (empirical) choice of $I_{out,0}$, α_P, α_I, and α_D, we obtained highly stable heating rates between 0.05 and 10 K/s ($\pm$ 0.05 %). The initial oszillations of the control loop damped out within < 0.5 s, which was important especially for multilayer CO and O_2 desorption studies, because both adsorbates possess substantial desorption rates already at 30 K. The here only briefly outlined method of a PC supported TD experiment was developed and in detail described by K.J. Schmidt [Sc02].

As an example for the performance of our experimental setup we present in Fig. 4.2 a TD spectrum of 3.3 ML krypton on Au(110)-(1×2). The three first-order desorption states of the first adlayer, γ, δ, and ε are well separated from the zero-order peaks of the second layer, β, and the third layer, α. The peaks α and β are clearly resolved, although separated by only 2.2 K.
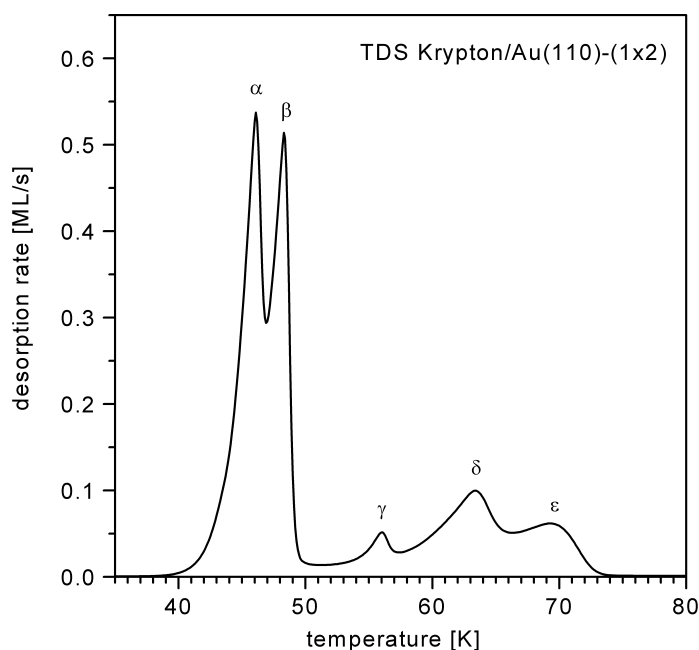

Fig. 4.2: TDS Kr/Au(110)-(1×2), taken with a heating rate of 1.00 K/s. Initial Kr coverage 3.3 ML. Spectrum as measured without smoothing, background subtraction, or any other refinement.

T EMPERATURE CALIBRATION FOR LOW-TEMPERATURE (LT) TD EXPERIMENTS – As already mentioned, the precise measurement of low temperatures with thermocouples is difficult. Due to the small Seebeck coefficients at low temperatures, small fluctuations in the reference temperature, T_{ref}, may lead to major temperature errors. T_{ref} should be as low as practically possible, e.g., l-N_2 instead of ice/water, since the impact of fluctuations in T_{ref} on U_{th} is proportional to S_K. Problems arise also, especially with the type K thermocouple, from large temperature gradients along the wire, which are likely to occur in LT experiments. The composition of the alloy changes from grain to grain. This leads, in the presence of a strong temperature gradient, to contributions to U_{th} which do *not* average out [Ko75], and which may change with the sample temperature. Another disadvantage of type K thermocouples is that their LT behaviour depends on the exact composition of the welding spot, so that calibration is necessary for each batch. Finally, the temperature of the welding spot may deviate from the actual sample temperature due to heat conduction through the thermocouple wires. These problems suggest as solution an in-situ calibration of the temperature measurement *under the conditions of the experiment*, which, in our case, is TDS. A suitable method, basing on a comparison of measured multilayer desorption energies, E_{des}, with tabulated sublimation enthalpies, ΔH_S, has been suggested by H. Schlichting et al. [Sc92, Sc93]. In the following, we briefly outline the thermodynamic and kinetic background of this procedure. What we need is a relation between E_{des}, the *kinetical* activation energy, and ΔH_S, the *thermodynamical* equilibrium heat of sublimation. The zero-order Polanyi-Wigner equation (PWE) establishes a relation between E_{des} and the desorption rate, R_{des}, and so does the Clausius-Clapeyron equation (CCE) with ΔH_S and the equilibrium vapour pressure, p(T):

$$E_{des} \leftrightarrow R_{des}(T) \qquad R_{des} \equiv -\frac{d\Theta}{dt} = \nu_0 e^{-(E_{des}/RT)} \quad \Rightarrow \quad \frac{d\ln R_{des}}{dT} = \frac{E_{des}}{RT^2} \quad \text{(PWE)}$$

$$? \updownarrow \; \Leftarrow \; \updownarrow \qquad\qquad\qquad\qquad\qquad\qquad\qquad\qquad\qquad\qquad\qquad\qquad \text{(Eq. 4.3)}$$

$$\Delta H_S \leftrightarrow p(T) \qquad\qquad\qquad\qquad\qquad\qquad \Rightarrow \quad \frac{d\ln p}{dT} = \frac{\Delta H_S}{RT^2} \quad \text{(CCE)}$$

It is clear from Eq. 4.3 that we can just as well ask for a relation between R_{des} and p. For this purpose, we consider the sublimation process with the fluxes of adsorbing, f_{ad}, and desorbing, f_{des}, particles. Under equilibrium conditions, the fluxes compensate: $f_{ad} = - f_{des}$. For f_{ad}, the collision flux (or Hertz-Knudsen) equation, multiplied with the sticking coefficient, S, applies:

$$f_{ad} \equiv \frac{dN_{ad}}{Adt} = \frac{1}{4}\frac{N}{V}\overline{v}S = \frac{p}{(2\pi m k_B T)^{1/2}}S = -f_{des} \; . \qquad\qquad\qquad \text{(Eq. 4.4)}$$

In Eq. 4.4, $\overline{v}$ denotes the mean thermal velocity, while the other symbols have their usual meaning. The crucial point is now to assume that the desorption flux under equilibrium conditions can be identified with the desorption rate at the same temperature under the conditions of the TDS experiment (where $f_{des} \gg f_{ad} \rightarrow 0$). This is the so-called quasi-equilibrium assumption [Kr91]:

$$\left| f_{des} \right| = \frac{N_{ML}}{A} R_{des} \tag{Eq. 4.5}$$

with the particle density at monolayer coverage, N_{ML}/A. (This factor is necessary because, for the sake of consistency, R_{des} has been defined as the negative change of the *relative* coverage, Θ.)

Combining Eqs. 4.4 and 4.5 we get:

$$p = \frac{1}{S} \frac{N_{ML}}{V} \left(2\pi m k_B T \right)^{\frac{1}{2}} R_{des} = const\ T^{\frac{1}{2}}\ R_{des}\ , \tag{Eq. 4.6}$$

which is the desired relation between p and R_{des}. We easily obtain by differentiation:

$$\frac{d\ln p}{dT} = \frac{d\ln R_{des}}{dT} + \frac{1}{2T}\ , \tag{Eq. 4.7}$$

and, with Eq. 4.3, the relation between E_{des} and ΔH_S:

$$\Delta H_S = E_{des} + \tfrac{1}{2} RT \tag{Eq. 4.8}$$

The difference of $(1/2)\,RT$ ($< 2\,\%$ of ΔH_S in our experiments) can be regarded as expansion (or volume) work. In a *pumped* UHV recipient, this term can be neglected. As the next step, we have to calculate ΔH_S at the multilayer desorption temperature, T_{des}. We start from tabulated values [An67] for ΔH_S at $T = 0$, $\Delta H_{S,T=0}$. At $T = 0$, no volume work can be exchanged, and, therefore, $\Delta H_{S,T=0} = \Delta U_{S,T=0}$. The sublimation enthalpy at the desorption temperature, $\Delta H_{S,T_{des}}$, can be calculated by integrating the difference of the heat capacities of the condensed phase, $C_{p,s}$, and the gas phase, $C_{v,g}$ (Eq. 4.9). For the gas, but not for the condensed phase, the difference between C_p and C_v is substantial. Here, we use $C_{v,g}$ instead of $C_{p,g}$, because no volume work is exchanged in a pumped recipient:

$$\Delta H_{S,T_{des}} = \Delta H_{S,T=0} + \int_{0}^{T_{des}} \left(C_{v,g} - C_{p,s}\right) dT'$$

$$= \Delta H_{S,T=0} + \tfrac{1}{2} R T_{des} \left(F_{trans} + F_{rot}\right) - \left(H_{s,T_{des}} - H_{s,T=0}\right)$$

(Eq. 4.9)

with the translational, F_{trans}, and (excited) rotational, F_{rot}, molecular degrees of freedom, and the tabulated [An67] enthalpy differences $H_{s,T_{des}} - H_{s,T=0}$ of the condensed phase.

For the practical T calibration, two parameters (ADC offset and gain) were systematically varied until E_{des} and ΔH_S coincided for a number of gases including CO ($T_{des} = 32$ K), O_2 ($T_{des} = 34$ K), Kr ($T_{des} = 44$ K, see Fig. 4.3) as shown in Table 4.1. For the less crucial calibration at higher temperatures, the whole sample, including sample holder and thermocouple, was immersed into l-N_2 (77.35 K), ice/water (273.16 K) and boiling water (373.16 K). After the described calibration, the temperature error was estimated to be less than ± 1 K at 28 K and ± 0.5 K at 273 K.
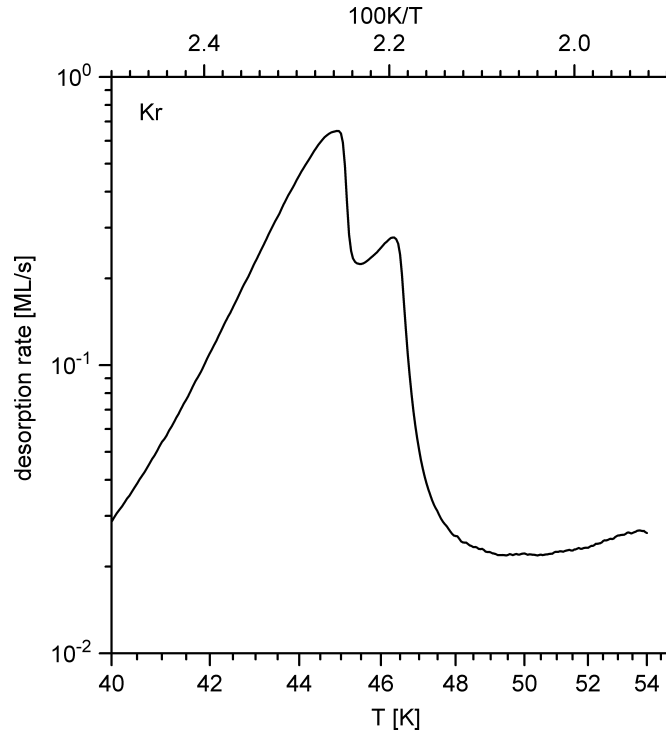

Fig. 4.3: Desorption trace for Kr multilayers (0.2 K/s). The peaks correspond to multilayer and 2nd layer desorption. The multilayer desorption energy amouts to 11.39 kJ/mol.

[kJ/mol]	CO (32 K)	O_2 (34 K)	Kr (44 K)
ΔH_S (calc.)	8.31	9.00	11.08
E_{des} (exp.)	8.31	8.90	11.39

Table 4.1: Calculated sublimation enthalpies and measured desorption energies in the context of the temperature calibration.

4.1.3. Evaluation of the desorption activation parameter E_{des}, n, and ν_n

In the literature, several methods for evaluating the desorption activation parameters E_{des}, ν_n, and n have been described. For a critical comparison, see the article by de Jong et al. [Jo90]. These methods can be arranged according to the fraction of each spectrum employed for the data evaluation: a single point, a small part of the curve, or the whole curve. In the same order, the methods become increasingly sensitive towards errors and inconsistencies of the measurement, e.g., erroneous overcrossing of the curves, background intensity, temperature errors, variations of the heating rate, etc.

THE POSITION OF THE DESORPTION MAXIMUM: HEATING RATE VARIATION AND REDHEAD'S FORMULA – The temperature of maximum desorption, T_{max}, measured as a function of the heating rate, β, allows the determination of E_{des} and ν_n, if the desorption order n is known. Using only one point of each peak, this method is not economical in respect of the data material, but it easily manages overlapping peaks. Therefore, it is particularly attractive for studies in which the substrate provides several desorption states which are saturated, for example in supported catalysts, or which become simultaneously occupied, for example in sputter deposition experiments as described in Chapter 7. The method requires a number of spectra taken for the same initial coverage, but at different heating rates. In the following, we derive a relation between T_{max}, β and the activation parameters E_{des}, ν_n, and n under the assumption that the latter are independent of coverage or temperature.

Differentiation of Eq. 4.1 with respect to temperature and setting the result equal to zero yields the following equation containing the temperature at maximum desorption T_{max}:

$$\frac{E_{des}}{RT_{max}^2} = \frac{\nu_n}{\beta} \, n \, \Theta_{max}^{n-1} \, \exp\left(-\frac{E_{des}}{RT_{max}} \right) \qquad \text{(Eq. 4.10)}$$

with $\Theta_{max} \equiv \Theta(T_{max})$. This equation can be rearranged as follows:

$$\ln\frac{\widetilde{T}_{max}^2}{\widetilde{\beta}} = \frac{E_{des}}{RT_{max}} + \ln\frac{\widetilde{E}_{des}}{\widetilde{\nu}_n\,\widetilde{R}\,n} + (1-n)\ln\Theta_{max} \quad . \tag{Eq. 4.11}$$

The tilde denotes division by an appropriate unit. According to Eq. 4.11, plots of $\ln(\widetilde{T}_{max}^2 / \widetilde{\beta})$ vs. $1/T_{max}$ as displayed in Fig. 6.7 are linear if the desorption behaviour is consistent with Eq. 4.1 and if the activation parameters are constant. From the slope and intercept of the best fit, the desorption energies E_{des} and the frequency factors ν_n can be determined. This method is particular convenient for 1st-order desorption, since the coverage-dependent term on the right hand side of Eq. 4.11 vanishes for $n = 1$.

Redhead [Re62] proposed a relation for estimating desorption energies from a single TD trace. The formula simply converts T_{max} into E_{des} for 1st-order desorption. The only requirement – and the main source of error – is a reasonable estimate for the frequency factor ν_1. Rearranging Eq. 4.10 for $n = 1$ we obtain:

$$E_{des} = RT_{max}\left[\ln\frac{\nu_1 T_{max}}{\beta} - \ln\frac{E_{des}}{RT_{max}}\right] \quad . \tag{Eq. 4.12}$$

The second term in the brackets is small compared to the first one and is approximated by $\ln(E_{des}/RT_{max}) = 3.64$, leading to an error $< 1.5\%$ for $10^8 < \nu_1/\beta < 10^{13}\,K^{-1}$.

L E A D I N G   E D G E   A N A L Y S I S – The leading edge analysis, as suggested by Habenschaden and Küppers [Ha84], allows to evaluate coverage-dependent (and even temperature-dependent) activation parameters. In order to fix Θ and T at the same time, the analysis is carried out for a small section on the low-temperature side of each spectrum. For this section, $\ln\widetilde{R}_{des}$ is plotted vs. $1/T$. According to Eq. 4.1, rearranged to

$$\ln\widetilde{R}_{des} = -\frac{E_{des}}{RT_{max}} + \ln\widetilde{\nu}_n + n\ln\widetilde{\Theta} \quad , \tag{Eq. 4.13}$$

this procedure should result in a straight line with the slope E_{des}/RT_{max} and an intercept that depends on ν_n. The analysed section was limited by the condition that only $\leq 5\,\%$ of the initial coverage were allowed to desorb.

The only possible disadvantage of this method is the small signal/noise ratio of the spectra in the range which is used for the analysis, but it does, according to our experience, deliver more reliable results than the 'complete' methods.

SEARCH FOR A LINEAR PLOT OF THE TD SPECTRUM − According to Eq. 4.1, rearranged to:

$$\ln\frac{\widetilde{R}_{des}}{\widetilde{\Theta}^n} = -\frac{E_{des}}{RT} + \ln\widetilde{\nu}_n \ , \qquad\qquad\text{(Eq. 4.14)}$$

a plot of $\ln\left(\widetilde{R}_{des}/\widetilde{\Theta}^n\right)$ vs. $1/T$ should be linear for a proper choice of the desorption order n. If n is chosen too small, the resulting curve shows a concave shape around the desorption maximum (and vice versa). Average values of E_{des} and ν_n can be obtained from the slope and the intercept of the linear plot. If no linear plot can be found, then E_{des} and ν_n are strongly coverage-dependent or the desorption kinetics is more complex than presupposed by Eq. 4.1. [Jo90, Pa90a]. An example for a non-linear plot is displayed in Fig. 6.5b.

COMPLETE METHODS − These methods, suggested independently by Bauer and Todd [Ba75] and King [Ki75], analyse complete TD coverage series. They employ different formalisms, but they lead to identical results. Here, we describe King's method because it is more intelligible: For a fixed *residual* coverage, Θ_i, we extract temperature-rate pairs $[R_{des}(\Theta_i), T(R_{des}(\Theta_i))]$ from a series of TD spectra with different *initial* coverages and plot $\ln R_{des}(\Theta_i)$ vs. $1/T(R_{des}(\Theta_i))$. According to the logarithmic form of the Polanyi-Wigner equation,

$$\ln\widetilde{R}_{des}(\Theta_i) = -\frac{E_{des}(\Theta_i)}{RT(\Theta_i)} + \ln\widetilde{\nu}_n(\Theta_i) + n\ln\widetilde{\Theta}_i \ , \qquad\qquad\text{(Eq. 4.15)}$$

the slope of this (linear) plot is proportional to E_{des}. If the desorption order, n, is known, the frequency factor, ν_n, can be evalutated from the intercept. This procedure can be repeated for all desired coverages Θ_i. The complete methods are less sensitive towards noise than the leading edge analysis. However, typical measurement errors in the TD series, e.g., no ideal coincidence of the curves of already saturated peaks and overcrossing curves, mas cause misleading results.

ORDER PLOTS − According to the logarithmic form of the Polanyi-Wigner equation (Eq. 4.15), plots of $\ln\widetilde{R}_{des}(\Theta)\big|_{T_i}$ vs. $\ln\widetilde{\Theta}\big|_{T_i}$ for various fixed temperatures T_i are linear, if E_{des} and ν_n are independent of coverage. The slope equals the desorption order, n. An example is presented in Fig. 6.3.

4.1.4. Desorption kinetics of two-dimensional many-phase systems

Despite its simplicity, the Polanyi-Wigner equation (Eq. 4.1) provides an appropriate description of numerous desorption systems. There is, however, a class of systems with deviating behaviour. These systems can be understood by assuming that the desorption process is accompanied by a simultaneous two-dimensional (2D) phase equilibrium on the surface. In this section, we will restrict our attention to cases in which the phase equilibrium between 2D condensed and 2D gas phases leads to (a) auto-inhibition and (b) zero-order desorption. Furthermore, we discuss chemisorbed systems, which are of particular importance for this work (cf. Section 6.2.2) and show a behaviour between the two limiting cases (a) and (b). We exclude those (more complicated) cases in which the equilibration reactions on the surface, e.g. diffusion processes, are not sufficiently fast to maintain the 2D equilibrium during desorption. The successful treatment of such systems is the achievement of Kreuzer and Payne [Kr88a].
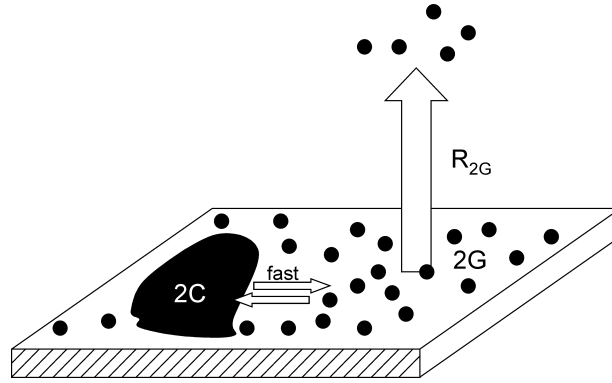

Fig. 4.4: Two-phase system with a chemical equilibrium between a 2D condensed phase (2C) and a 2D gas phase (2G). The local desorption rate from 2G is given by R_{2G}. No desorption is assumed to occur from 2C ($R_{2C} = 0$).

A U T O - I N H I B I T I O N – We consider a 2D two-phase system, consisting of a 2D condensed phase, 2C, and a 2D gas phase, 2G, with equal chemical potential, $\mu_{2G} = \mu_{2C}$, i.e., with a phase equilibrium established between both 2D phases (Fig. 4.4).

The local desorption rate from 2G is R_{2G}, whereas no desorption occurs from R_{2C}.[1] The desorption rate of the 2D gas phase, R_{2G}, is given by the Polanyi-Wigner equation:

$$R_{2G} = \nu_{2G} \Theta_{2G}^{n} \exp\left(-\frac{E_{des}(2G)}{RT}\right) \qquad \text{(Eq. 4.16)}$$

---

[1] In the next paragraph it will be shown that the condition $R_{2C} = 0$ is equivalent to a vanishing sticking coefficient for adsorption on 2C, i.e., $S_{2C} = 0$.

The total rate, R_{tot}, which is the measured quantity, depends on the local rate, R_{2G}, and on the surface fraction covered by 2G, F_{2G}:

$$R_{tot} \equiv -\frac{d\Theta_{tot}}{dt} = R_{2G}F_{2G} = R_{2G}(1-F_{2C}) \qquad \text{(Eq. 4.17)}$$

with the surface fraction of 2C:

$$F_{2C} \equiv \frac{A_{2C}}{A_{tot}} = \frac{\Theta_{tot}-\Theta_{2G}^{crit}}{\Theta_{2C}-\Theta_{2G}^{crit}} \quad \text{for} \quad \Theta_{tot} > \Theta_{2G}^{crit} \quad \text{and} \quad F_{2C} = 0 \quad \text{else.} \qquad \text{(Eq. 4.18)}$$

A_{tot} and A_{2C} denote the total area and the area covered by 2C, respectively. Θ_{tot} is the total coverage. The local coverages of the respective phases in equilibrium are given by Θ_{2C} and Θ_{2G}^{crit}. Θ_{2G}^{crit} is the critical coverage of 2G, i.e., island formation is not possible for $\Theta_{2G} < \Theta_{2G}^{crit}$:

$$\Theta_{2G} = \begin{cases} \Theta_{2G}^{crit} & \text{(with islands)} \\ < \Theta_{2G}^{crit} & \text{(without islands)} \end{cases} . \qquad \text{(Eq. 4.19)}$$

The total coverage, Θ_{tot}, is given by:

$$\Theta_{tot}(t) = \Theta_{initial} + \int_0^t \frac{d\Theta_{tot}}{dt'} dt' . \qquad \text{(Eq. 4.20)}$$

The equation system (4.16) - (4.20) was numerically integrated for the following parameters: $E_{des}(2G) = 130$ kJ/mol, $\nu = 10^{13}$ s^{-1}, $\Theta_{2G}^{crit} = 0.25$ ML, $n = 1$. The resulting curves for a variety of different initial coverages $\Theta_{initial}$ are plotted in Fig. 4.5. The curves indicate ordinary first-order desorption up to the critical coverage of 0.25 ML. For higher $\Theta_{initial}$, the peaks shift to higher temperatures and become very narrow – indications that the desorption reaction is increasingly auto-inhibited. The reason for this behaviour is that the phase from which desorption occurs, 2G, is increasingly replaced by the condensed phase, 2C, with $R_{2C} = 0$. Formally, a criterion for auto-inhibition is a negative overall desorption order, which is also observed in the present case, as shown in Fig. 4.5b by the convex curvature of the high-coverage leading edges. In contrast, the first-order curves for $\Theta_{initial} < 0.25$ ML show a concave shape, whereas zero-order desorption would lead to a linear plot (see Fig. 4.9 for comparison).
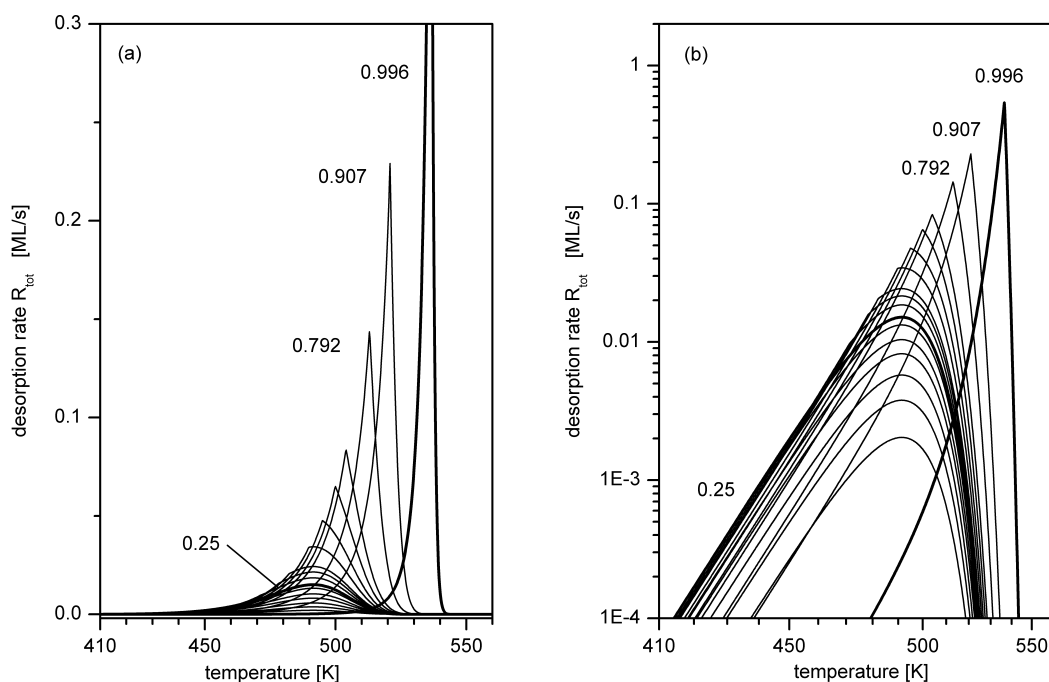
32

Fig. 4.5: Results of a numerical integration of Eqs. 4.16 - 4.20. See the text for the values of the parameters. The t-abscissa was converted into a T-abscissa by applying a heating rate of $\beta = dT/dt = 1$ K/s. (a) Linear plot. (b) Logarithmic plot over a reciprocal T scale.

ZERO-ORDER DESORPTION – For understanding the existence of zero-order kinetics in the case of sub-monolayer desorption, several authors, e.g., Nagai et al. [Na84], Asada and Masudo [As89], and Kreuzer and Payne [Kr88a], introduced a third 2D phase, which was assumed to consist of a 2D gas phase on top of the condensed phase (2C). This new phase, 2GC in abbreviation, is in equilibrium with 2C and with the gas phase on the substrate surface, 2GS, and it allows desorption from the sample area covered by 2C (see Fig. 4.6).

The question arises whether there is any relation between the rate from 2GS, R_{2GS}, and the rate from 2GC, R_{2GC}. Several authors claim that the equality of the chemical potentials in equilibrium, $\mu_{2GC} = \mu_{2GS}$, leads to equal rates, $R_{2GS} = R_{2GC}$ [Na84, Le01]. However, a closer inspection of the problem on the basis of the quasi-equilibrium assumption leads to the conclusion that the rates have the same ratio as the sticking coefficients for adsorption on the respective phases[2]. This is illustrated in Fig. 4.7, where we assume that the 2D phases are in equilibrium with each other and with a 3D gas phase (3G). The particle flux onto the surface, f_{ad}, is given by the collision flux (or Hertz-

---

[2] The following concise treatment bases on the work of Kreuzer and coworkers [Kr88, Kr91], which extensively applied quasi-equilibrium considerations to thermal desorption. In contrast, the original approach of Asada and Masudo employed transition state theory. This treatment predicted equal rates for both 2D gas phases if the following assumption were made: (a) equilibrium between all 2D phases, (b) no activation barrier for adsorption, (c) transmission coefficient κ equal for desorption from 2GS and 2GC (see Eyring equation, Eq. 3.8). Assumption (b) excludes many cases of chemisorption.

Knudsen) equation (Eq. 4.4). While f_{ad} is spatially constant, this is not necessarily the case for the adsorption rate, R_{ad}, because R_{ad} depends on the sticking coefficient, S, which may vary for the particular 2D phases. R_{ad} is, in equilibrium, *locally* compensated by the desorption flux, R_{des}:

$$R_{ad} \equiv \frac{dN_{ad}}{Adt} = Sf_{ad} \quad = \quad -R_{des} \equiv \frac{dN_{des}}{Adt}$$ (Eq. 4.21)

Thus, for each 2D phase holds:

$$\frac{R_{des,i}}{S_i} = -f_{ad} = const .$$ (Eq. 4.22)

In order to apply these consideration to thermal desorption, we assume that the desorption fluxes in the TDS experiment, in which the phase 3G is absent, are equal to the respective fluxes in the case of an equilibrium situation between adsorbate and 3D gas (quasi-equilibrium assumption).
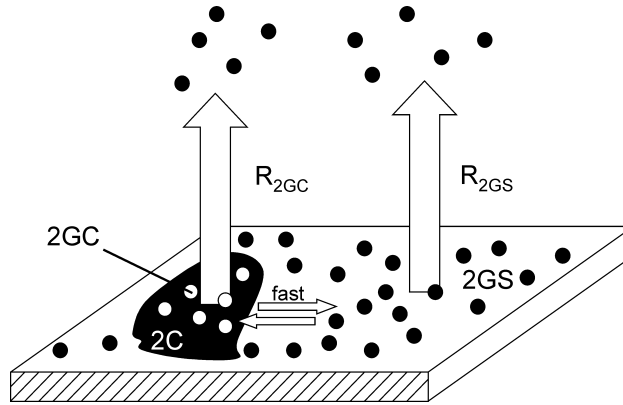

Fig. 4.6: Two-dimensional three-phase system with a 2D condensed phase (2C), a 2D gas phase on the substrate (2GS), and a 2D gas phase on the condensed phase (2GC). The local desorption rates from 2GS and 2GC are R_{2GS} and R_{2GS}, respectively.
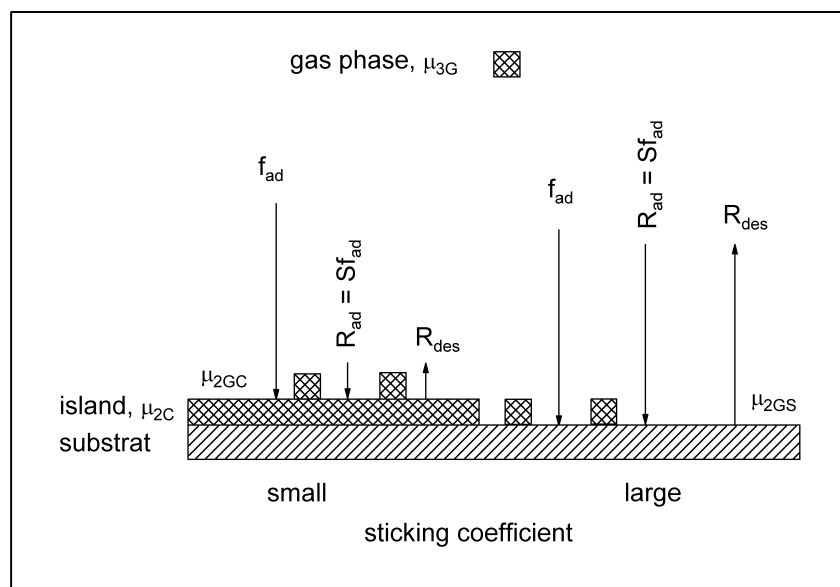
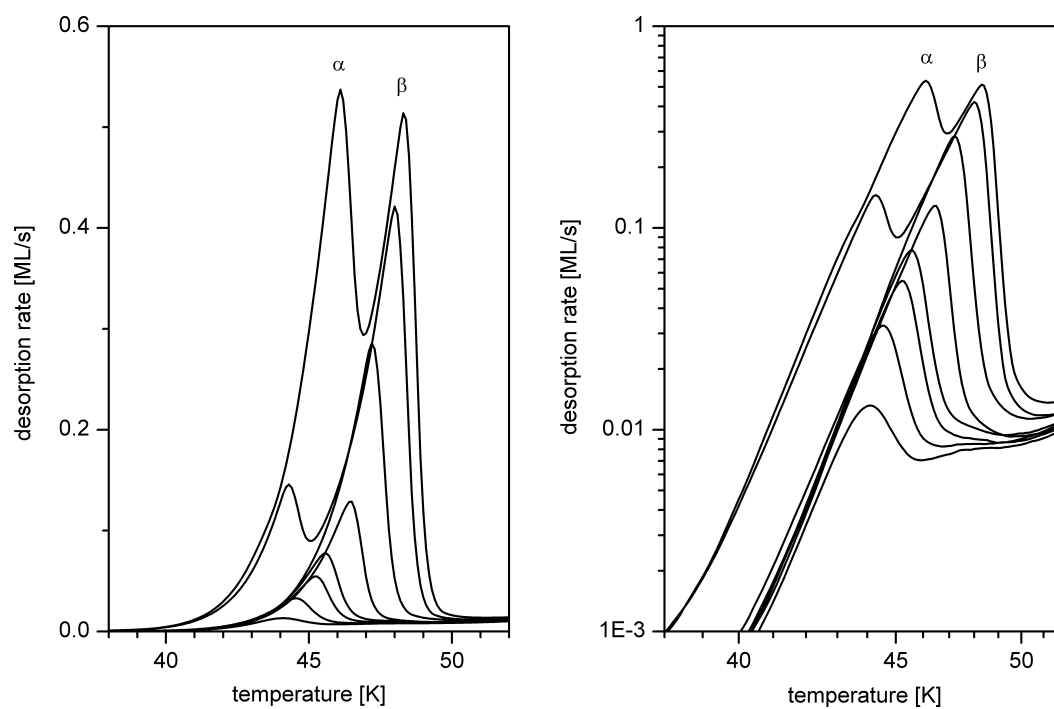Fig. 4.7: Desorption from two phases with different sticking coefficients. See text for further explanations.

Fig. 4.8: Experimental thermal desorption spectra of Kr on Au(110)-(1×2). Both the second-layer peak β and the multilayer peak α show zero-order desorption kinetics. Heating rate 1.00 K/s. The monolayer peaks are not displayed; see Fig. 4.2 for a complete spectrum.

Typical systems showing zero-order desorption kinetics are adsorbates of metal atoms[3] and physisorbed gases on solid surfaces (Fig. 4.8). Common to these systems is a high sticking probability, which is often close to unity regardless of whether the particles impinge on already existing adsorbate islands (which represent the 2D condensed phase) or on the substrate. If the sticking coefficients are equal for both 2D gas phases, then the desorption rate is, according to Eq. 4.22, equal for all 2D gas phases. Together with the fact that the phase equilibrium keeps the local coverages, Θ_{2GC} and Θ_{2GS}, constant, these conditions lead necessarily to zero-order desorption as long as the phase equilibrium persists.

In order to demonstrate the occurrence of zero-order desorption, we calculated the total desorption rate

$$R_{tot} \equiv -\frac{d\Theta_{tot}}{dt} = R_{2GC}F_{2C} + R_{2GS}(1 - F_{2C}) \qquad \text{(Eq. 4.23)}$$

with F_{2C} as given by Eqs. 4.18-4.20. The local desorption rates, R_{2GS} and R_{2GC}, are determined by the Polanyi-Wigner equation (Eq. 4.16). Under the condition mentioned above, $S_{2GC} = S_{2GS}$, the local rates are equal, $R_{2GC} = R_{2GS} \equiv R_{2G}$. As a result, the total rate is independent of F_{2C}, and Eq. 4.23 is reduced to:

$$R_{tot} = R_{2G} = \nu_{2GC}\Theta_{2GC}^n \exp\left(-\frac{E_{des}(2GC)}{RT}\right) = \nu_{2GS}\Theta_{2GS}^n \exp\left(-\frac{E_{des}(2GS)}{RT}\right) \quad \text{(Eq. 4.24)}$$

Since the local coverages do not change with time as long as $F_{2C} > 0$, Eq. 4.24 indeed describes zero-order desorption[4].

The results of a numerical solution of Eq. 4.23 is displayed in Fig. 4.9. The same parameters as in the preceding section were employed. As expected, the curves share a common leading edge as long as the 2D phase equilibrium is established, i.e., if the total coverage exceeds 0.25 ML.

---

[3] For an exhausitve (and, partially, exhausting) discussion of such systems, see Ref. [Wa03].

[4] Strictly speaking, this conclusion holds only for isothermal desorption, since the 2D equilibrium constant and, therefore, the local coverages of the 2D gas phases are temperature-dependent. These changes in the local coverages will influence the total rate, if they are not compensated by changes in ν or E_{des}. In other words, a deviation from perfect zero-order desorption may occur in the (non-isothermal) TD experiment.
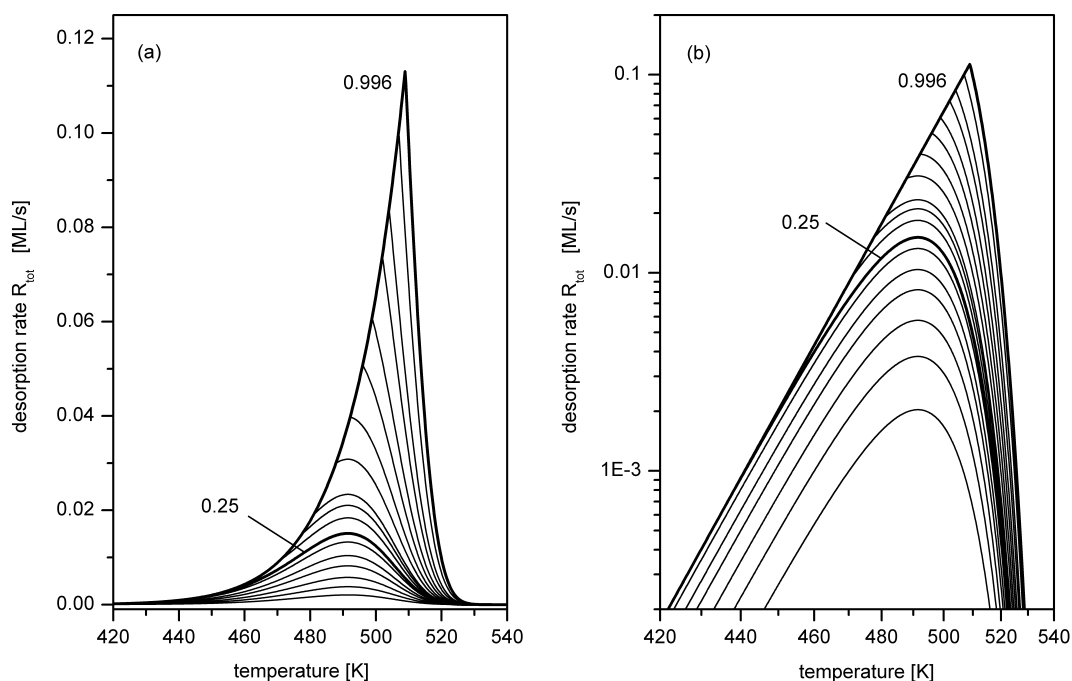
Fig. 4.9: Numerical solution of Eq. 4.23 under consideration of Eqs. 4.18 - 4.20. We used the same parameters as in Fig. 4.5. The t-abscissa was converted into a T-abscissa by applying a heating rate of $\beta = dT/dt = 1$ K/s. (a) Linear plot. (b) Logarithmic plot over a reciprocal T scale.

The question arises whether the assumption of a third 2D phase is a necessary condition for zero-order desorption, or, in other words, whether the occurrence of zero-order desorption kinetics proves the existence of a 2D gas phase on top of the 2D condensed phase (2GC). In the here presented form, the model bases only on two assumptions: (a) the chemical potentials of the 2D phases are equal (i.e., the phase equilibrium is established) and (b) the local sticking coefficients determine the local desorption rates. In this consideration, all properties of the 2GC phase (e.g, sticking coefficient, coverage, desorption energy and frequency factor) can be ascribed to the condensed phase itself.

Zero-order desorption only proves that the surface is completely covered by a number of adsorbate phases with equal chemical potential and sticking coefficient. Deviation from zero order at a certain coverage allows to determine the critical coverage for the formation of a phase equilibrium. This critical coverage may depend on temperature. By a systematic variation of the heating rate, which influences the temperature range of desorption, the phase diagram of the particular adsorbate system can be determined [Wa03]. No further information about the number and the type of phases can be derived from the fact of zero-order desorption.

We emphasized that it is *not* true that "zero-order desorption must generally be observed in any kind of phase equilibrium", an assertion that was frequently made by Nagai (see, for example, [Na84, Na87]). Thus, deviation from zero-order desorption does *not* prove that the 2D equilibrium is not established, as we will demonstrate in the next section.

CHEMISORBED SYSTEMS WITH WEAK AUTO-INHIBITION – In chemisorbed two-phase systems the sticking coefficient for adsorption on the 2D condensed chemisorbed phase (2C) is lower than for adsorption on the substrate (but it may be > 0). With Eq. 4.22 follows that the local desorption rate from 2C, R_{2C}, is lower than the rate from the 2D gas phase on the substrate (2G), R_{2G}. The different local rates are illustrated in Fig. 4.10.
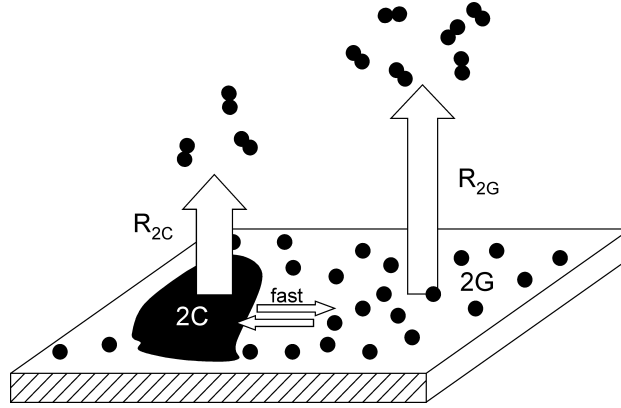

Fig. 4.10: Desorption from a chemisorbed two-phase system with a 2D condensed phase (2C) and a 2D gas phase (2G). Local desorption rates from 2G and 2C are given by R_{2G} and R_{2C}, respectively. The desorption process is assumed to be associative.

Similar to the preceding case of zero-order desorption, the total desorption rate can be calculated by:

$$R_{tot} \equiv -\frac{d\Theta_{tot}}{dt} = R_{2C}F_{2C} + R_{2G}(1 - F_{2C})$$

(Eq. 4.25)

with F_{2C} given by Eq. 4.18. For calculating the local rates, R_{2C} and R_{2G}, which are not equal, we employed again the Polanyi-Wigner equation:

$$R_{2G} = \nu_{2G}\Theta_{2G}^{n_{2G}} \exp\left(-\frac{E_{des}(2G)}{RT}\right)$$

(Eq. 4.26a)

$$R_{2C} = \nu_{2C}\Theta_{2C}^{n_{2C}} \exp\left(-\frac{E_{des}(2C)}{RT}\right)$$

(Eq. 4.26b)

The results of a numerical solution of Eq. 4.25 is displayed in Fig. 4.11. For the 2D gas phase (2G) we applied the following parameters[5]: $n_{2G} = 2$, $E_{des}(2G) = 140$ kJ/mol, and $\nu_2(2G) = 9.5 \times 10^{-3}$ cm^2/s. And for 2C: $n_{2C} = 2$, $E_{des}(2C) = 151$ kJ/mol, and $\nu_2(2C) = 6.8 \times 10^{-3}$ cm^{2}s^{-1}. The local coverage of 2G, which equals the critical coverage, was 0.35 ML; the local coverage of 2C 1.0 ML. These parameters imply that the sticking coefficient on 2C is approximately half the sticking coefficient on 2G, i.e., $S_{2C}/S_{2G} = R_{2C}/R_{2G} = 0.52$ at 550 K.

Comparison of the curves in Fig. 4.11 with those in Figs. 4.5 and 4.9 shows that different local rates lead to an auto-inhibition effect. However, this effect is less pronounced as in the case of zero desorption from one phase. A closer inspection of the logarithmic plot in Fig. 4.11b reveals that the leading edges of the high-coverage spectra have still a convex shape. This curvature proves that the overall desorption order is negative and that the reaction is indeed auto-inhibited.

The three considered examples show that desorption with a simultaneous 2D phase equilibrium leads to auto-inhibition, if the local sticking coefficients differ, and to zero-order desorption, if all phases possess the same sticking coefficient.
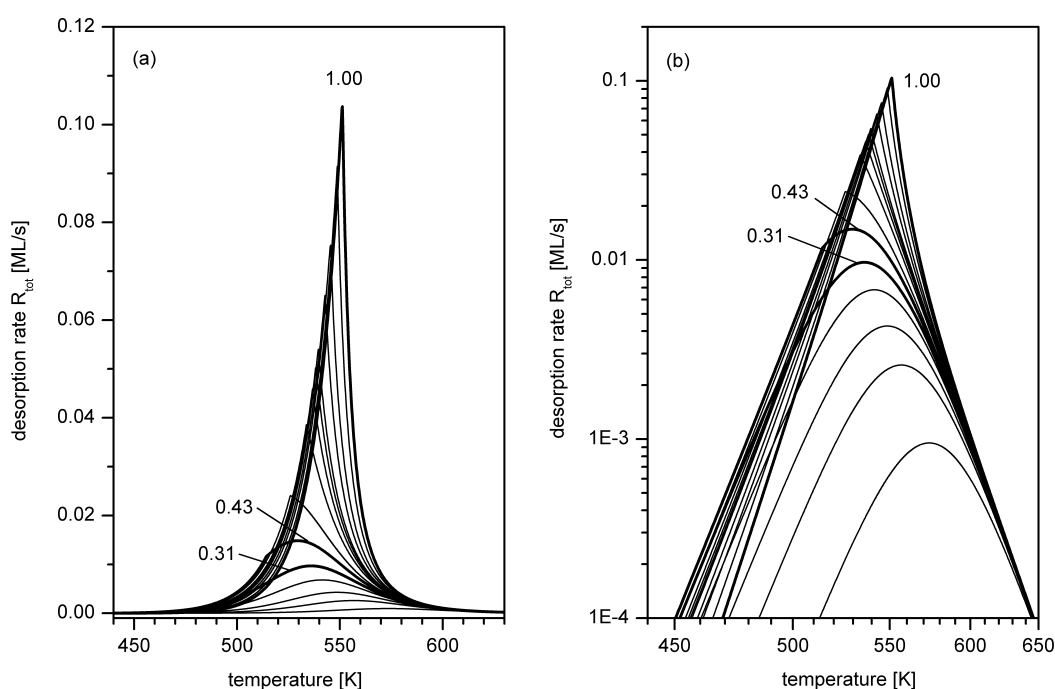

Fig. 4.11: Numerical solution of Eq. 4.25. Desorption activation parameters as listed in the text. The t-abscissa was converted into a T-abscissa by applying a heating rate of $\beta = dT/dt = 2.0$ K/s. (a) Linear plot. (b) Logarithmic plot over a reciprocal T scale.

---

[5] In this example, we use the same parameters as for chemisorbed oxygen on Au(110)-1×2). This desorption system is in detail analysed in Chapter 6.

4.1.5. The compensation effect

The compensation effect, a mutual compensation of changes in the activation energy and the frequency factor, frequently occurs in surface reactions including thermal desorption. A typical example is provided by our O_2/Au thermal desorption spectra in Fig. 5.1. The desorption energy E_{des}, displayed in Fig. 5.2a, depends on coverage and decreases by $\approx$20% between 0.5 and 1.0 ML. At a constant frequency factor of $\approx k_B T/h$, this change of E_{des} would shift the α_2 peak gradually from 45 K to 37 K. Actually, the position of α_2 is constant due to a simultaneous decrease of the frequency factor (Fig. 5.2b), which compensates the change of E_{des}.
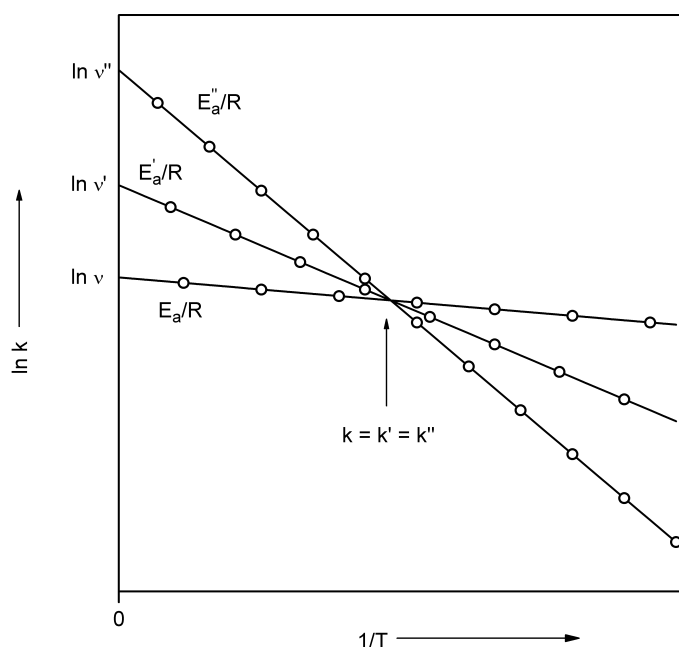

Fig. 4.12: The compensation effect in the Arrhenius plot representation.

If k and k' denote the desorption rate constants at two different coverages, this result can be expressed as $k(\nu,E) = k'(\nu',E')$. With the Arrhenius equation follows:

$$\nu e^{-\frac{E}{RT}} = \nu' e^{-\frac{E'}{RT}} \quad \text{or} \quad d\ln\nu = -\frac{dE}{RT} \quad . \qquad \text{(Eq. 4.27)}$$

This is the condition for the compensation effect. In the ln k vs 1/T diagram Fig. 4.12, also called Arrhenius plot, the compensation effect leads to a straight line rotating around a point at which k remains unchanged while ν and E_{des} vary. This point defines the so-called isokinetic temperature.

40

In the following, we give a simple explanation of the compensation effect on the example of thermal desorption. An adatom, A, has a binding energy of $E_{A-S} \approx E_{des}$ and vibrates perpendicular to the surface, S, with the frequency ω. A weakening of the A-S bond, for example due to a coverage increase, is usually accompanied by a decrease of ω. A lower frequency leads to a higher contribution of this vibration to the adsorbate partition function, Q_{ads}. If we – reasonably – assume that the transition-state partition function, $Q_{-1}^{\neq}$, is not affected by these changes, than the Eyring equation predicts a decrease of the frequency factor, ν. However, this decrease of ν, which should lower the desorption rate, is compensated by the increased exponential term containing a lower desorption energy of the weakened bond. For a closer inspection of this result, we combine the (empirical) Arrhenius and the (theoretical) Eyring equation (see Eqs. 3.7 and 3.8):

$$ k_{des} = \nu \, e^{-\frac{E_{des}}{k_B T}} = \frac{k_B T}{h} \frac{Q_{-1}^{\neq}}{Q_{ads}} e^{-\frac{E_0}{k_B T}} \qquad . \tag{Eq. 4.28} $$

If we assume $E_0 \approx E_{des}$, we can identify ν with the ratio of the partition functions multiplied with the universal frequency factor, $k_B T/h$. Inserting Q_{ads}, which is simply the partition function of the considered adsorbat-substrat vibration, leads to:

$$ k_{des} = \frac{k_B T}{h} Q_{-1}^{\neq} \left(1 - e^{-\frac{\hbar \omega}{k_B T}} \right) e^{-\frac{E_0}{k_B T}} \qquad . \tag{Eq. 4.29} $$

The term in brackets increases exponentially with growing ω, whereas the final exponential term decreases with increasing E_0, i.e., a compensation effect will occur if there is an approximate proportionality between ω and E_{des}.[6]

There is no chance of establishing a general relationship between both quantities. ω depends on the curvature of the potential energy curve at the minimum:

$$ \omega = \left(\frac{\kappa}{\mu} \right)^{\frac{1}{2}} \quad \text{with} \quad \kappa = \left(\frac{\partial^2 U}{\partial r^2} \right)_{r=r_0} \qquad , \tag{Eq. 4.30} $$

[6] Extension of the argument to other degrees of freedom than the A-S (stretching) vibration is straight-forward. In the case of localized adsorption, a reduced E_{des} will be accompanied by a softening of the two bending modes (frustrated translations), which has the same effect as the softening of the stretching mode. For a (partially) mobile adsorbate, the translational partition function increases with decreasing E_{des} and influences k_{des} in the same way.

(with the reduced mass μ) while E_{des} is the depth of the potential well. However, experience shows that they usually depend on each other in the above-mentioned way. It is easy to see way this must be so, if another quantity, the bond length, D, comes into play. With increasing bonding energy and frequency, the bond length decreases. This fact is nicely illustrated by the molecular ions of O_2:

	D(Å)	ω (cm^{-1})
O_2^{2-}	1.49	802
O_2^-	1.33	1097
O_2	1.21	1580
O_2^+	1.12	1905

Table 4.2: Bond lengths and vibrational frequencies of O_2 and its molecular ions. After [Va76].[7]

Eq. 4.30 and Table 4.2 show that the curvature at the minimum decreases drastically (by a factor of $\approx$6), if the anti-bonding π* orbitals contain four electrons in O_2^{2-} instead of only one in O_2^+. The consequence for the relation between dissociation energy and ω is illustrated by the schematic potential energy curves in Fig. 4.13. This figure shows a steep curve with an early minimum (representing O_2^+) and a shallow curve with a late minimum (O_2^{2-}). The dotted line is a curve with the depths and the minimum's position of the O_2^+ curve, but with the curvature of the O_2^{2-} curve. This curve shows a wrong behaviour for $r \to 0$, since it is not sufficiently repulsive, and it describes an unrealistic long-range interaction for large r. The figure makes clear that repulsion and range are the boundery conditions which demand that a deep potential curve is also steep. Accordingly, a strong bond with a high dissociation energy is accompanied by a hard vibration and *vice versa*. Thus, the occurence of a compensation effect in dissociation reactions such as thermal desorption[8] should be the rule, not the exception, a result that agrees with experimental observations.

---

[7] The corresponding dissociation energies are not available for all species. O_2^{2-} is not stable in the gas phase ($\omega = 0$), but exists in ionic crystals such as Na_2O_2, in which the anion carries probably less than two negative charges.

[8] The activation barrier of a reaction is caused by the intermediate dilatation and cleavage of chemical bonds. For example, the activation energy for the surface reaction $CO(ad) + O(ad) \to CO_2(ad)$ is mainly expended on the cleavage of the surface chemical bonds of $CO(ad)$ and $O(ad)$. Thus, also in such surface reactions a compensation effect should be – and is – observed.
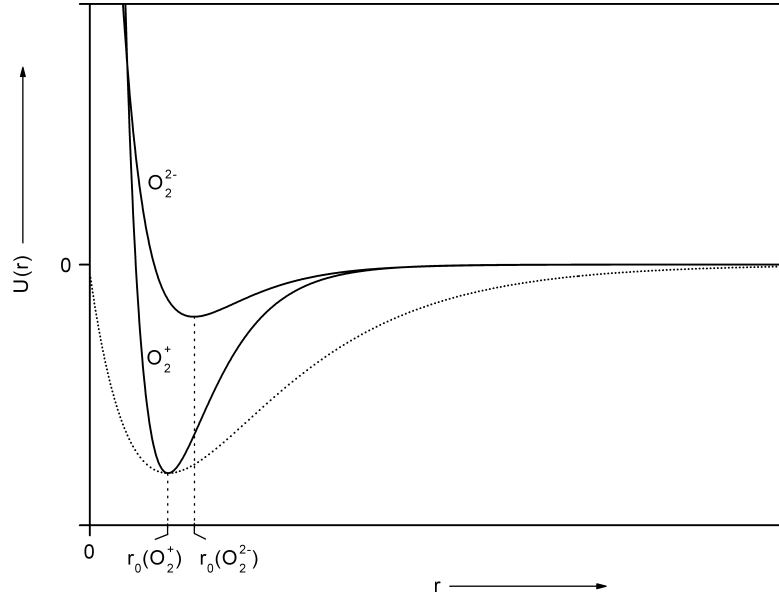
Fig. 4.13: Schematic Morse potential curves for O_2^+ and O_2^{2-} (solid lines). The curvatures of this curves have a ratio that agrees with the frequencies in Table 4.2. The dotted line was obtained by deepening the potential for O_2^{2-} without changing the curvature (and a shift from the minimum position of O_2^{2-} to that of O_2^+. The resulting potential is unrealistic for $r \to 0$ and $r \to \infty$, illustrating the interdependence of ω and E_{des}. The curves were shifted on the energy scale so that $U(r \to \infty) = 0$ for all curves.

4.1.6. Determination of absolute coverages and sticking coefficients with TDS

A B S O L U T E   C O V E R A G E S, σ_i, were estimated by assuming that the intensity of the thermal desorption spectra, I_{QMS}, is proportional to the particle flux through the orifice in the separately pumped chamber which contained the mass spectrometer (QMS) (Eq. 4.31). In order to evaluate the proportionality constant, b, between this flux, f_{des}, and I_{QMS}, we recorded the mass spectrometer signals in the QMS chamber for several partial pressures, p_i, of the respective gas in the main chamber. The corresponding fluxes, f_i, through the orifice, calculated by the effusion (or Hertz-Knudsen) equation (Eq. 4.32), were plotted versus the I_{QMS} values. With the constant b determined, the instantaneous TDS signal can be related to the flux and, therefore, the integrated TDS intensity to the number of desorbed particles, N_{des}, which provides, together with the cross section of the orifice, A, absolute coverages (Eq. 4.33).

$$b\,I_{QMS} \quad = \quad f_{des} \equiv \frac{dN_{des}}{Adt} \qquad\qquad \text{(Eq. 4.31)}$$

$$b\,I_{QMS} \quad = \quad f_i \equiv \frac{dN_i}{Adt} = \frac{p_i}{\sqrt{2\pi m_i k_B T}} \qquad\qquad \text{(Eq. 4.32)}$$

43

$$\sigma_{des} \equiv \frac{N_{des}}{A} = b \int_0^\infty I_{QMS} dt \qquad (Eq.~4.33)$$

Since the calibration pressures p_i were measured by an ion gauge, the fluxes and, therefore, the absolute coverages have the same error as the pressure measurement ($< 20\,\%$). An additional systematic error leading to an over-estimate for absolute coverages may arise from re-adsorption during the TDS experiment.

QMS - PRESSURE OR FLUX DETECTOR? – Thermal desorption spectra can be measured either by flux or by partial pressure detection. The particle flux from the sample produces a partial pressure, which depends on volume and pumping speed[9] – quantities which are only approximately known. Thus, flux detection is a more direct and accurate way for quantitative TD measurements. Under the conditions of our experiment, i.e., with the particle detector mounted at the entrance of a separately pumped chamber, the QMS is a flux rather than a pressure detector and as such is sensitive to the molecular speed of the desorbing particles. Therefore, especially for determining absolute coverages we normalized all QMS signals by multiplying with $(T/298\,K)^{1/2}$ (assuming thermal equilibrium between gas and surface) to account for a decreased sensitivity to fast molecules[10]. For proving our assumptions, we studied Kr adsorption at a sample temperature of 28 K. First, we converted the exposure values into absolute coverages, $\sigma_{(ads)}$, using the collision flux equation. These 'coverage' values still contained the sticking coefficient, S, i.e., we actually determined an *upper* limit to $\sigma_{(ads)}$, $\sigma_{(ads)}/S \geq \sigma_{(ads)}$. Thereafter, we compared $\sigma_{(ads)}/S$, i.e., the maximum amount of *adsorbed* Kr atoms, with the coverage as determined by the TD spectra analysis as described above, $\sigma_{(des)}$, i.e., with the actual amount of *desorbed* Kr atoms. If we now assumed, in our TDS analysis, that the QMS detects a thermalized gas ($T_{gas} = 298$ K), the number of *desorbed* Kr atoms exceeded the maximum number of *adsorbed* atoms by a factor of ≈ 2. To be precise, the apparent sticking coefficient was $S = \sigma_{(des)}/(\sigma_{(ads)}/S) = 2.15$ (since $\sigma_{(ads)} = \sigma_{(des)}$, if no re-adsorption occurres during the TD experiment). Remarkably, this value nearly equals the factor $(T_{des}/298\,K)^{1/2} = (68\,K/298\,K)^{1/2} = 2.09$, with the desorption temperature T_{des} of the respective submonolayer peak. We concluded that a normalization with $(T/298\,K)^{1/2}$ is necessary in order to obtain reasonable values ($S \leq 1$) for the sticking coefficient. After normalization of the Kr TD spectra, we calculated $S = 0.97 \pm 0.10$.

---

[9] The pumping speed can even depend on pressure and on the recent history of the chamber, probably because of adsorption on the UHV chamber walls, which may be saturated with the respective adsorptiv or not. This explanation is supported by the fact that we observed a history-dependent pumping speed in the case of O_2 adsorption, but not for the residual gas CO.

[10] 298 K is the gas temperature during calibration and enters Eq. 4.32.

A FURTHER ERROR in the determination of absolute coverages by the method described above may result from the angular distribution of the desorption flux, which is proportional to $\cos^n\Theta$. The experimental setup ensures that all molecules desorbing from a certain sample area can reach the QMS, but only those desorbing normal to the surface reach it without wall collisions. Wall collisions, however, may change the molecular velocity of the particles and thereby influence the flux, as mentioned above. If the exponent n changes for the different peaks measured, than additional, but probably small uncertainties are introduced.

STICKING COEFFICIENTS – As mentioned above, sticking coefficients, S, were determined by comparing the number of adsorbed atoms, as calculated by the collision flux equation, with the number of desorbed particles as estimated with the described method. The (rather substantial) pressure error, Δp, drops out because it enters both of the independently determined coverage values, and the residual error is small (< 10 %). This is a considerable advantage because the sticking coefficients determined by LEED – as an alternative method – still contain Δp.

We conclude that for determining absolute coverages our method is a makeshift which was only employed for adsorbates without long-range order. However, for evaluating sticking coefficients our method is more precise than the LEED method.

4.2. UV photoelectron spectroscopy

4.2.1. Fundamental aspects

All varieties of photoelectron spectroscopy [Hü96] rely on the photoelectric effect, which was discovered by H. Hertz [He87] and extensively studied by J.J. Thompson[11] [Th99], P. Lenard[12] [Le00, Le02], and R.A. Millikan[13] [Mi16].

According to Einstein's[14] famous interpretation [Ei05], the emitted photoelectrons possess a kinetic energy, $E_{kin,j}$, of

$$E_{kin,j} = h\nu - E_{b,j}^{V}.$$ (Eq. 4.34)

---

[11] Nobel price for physics in 1906.

[12] Nobel price for physics in 1905.

[13] Millikan did not accept Einstein's theory, which he saw as an attack on the wave theory of light. He worked for ten years, until 1916, on the photoelectric effect, and he even devised techniques for scraping clean the metal surfaces inside the vacuum tube. For all his efforts Millikan found disappointing results: he confirmed Einstein's theory, measuring Planck's constant to within 0.5 % by this method. One consolation was that he was awarded a Nobel prize for physics in 1923 for this series of experiments.

[14] Nobel price for physics in 1921.

The electron binding energy with respect to the vacuum level, $E_{b,j}^V$, which is synonymous to the ionization potential, I_j, is the energy difference between the inital N electron state with the energy E_N and a corresponding final N-1 electron state j with the energy $E_{N-1,j}$. According to Koopmans'[15] theorem [Ko25], $E_{b,j}^V$ is approximately equal to the negative energy of the respective one-electron state, ψ_j, (or 'orbital' in the case of atoms or molecules):

$$E_{b,j}^V = E_{N-1,j} - E_N \cong -\varepsilon_j \ . \tag{Eq. 4.35}$$

In the case of solids, the electron binding energy, E_b^F, is usually measured with respect to the Fermi level, E_F:

$$E_b^F = E_b^V - e_0\varphi \ . \tag{Eq. 4.36}$$

The work function, φ, is a material constant and depends sensitively on surface properties, as described in Section 4.3.

Koopmans' theorem neglects relaxation effects in the molecular ion. Thus, an exact relation must contain an additional term with the (experimentally unaccessible) intramolecular relaxation energy ΔE_{relax}:

$$E_{b,j,gas}^V = E_{N-1,j} - E_N = -(\varepsilon_j + \Delta E_{relax}) \tag{Eq. 4.37}$$

In the case of adsorbed particles, the presence of the surface leads to additional energy contributions. The initial state orbital energies change due to the adsorption ($\Delta E_{initial}$), and the adsorbed molecular ion (final state) interacts with its image in the solid (ΔE_{final}):

$$E_{b,j,ad}^F = E_{b,j,gas}^V - (\varphi + f\,\Delta\varphi) + \Delta E_{initial} + \Delta E_{final} \ , \tag{Eq. 4.38}$$

with $E_{b,j,gas}^V$ referenced to the vacuum level, E_{vac}. The constant f, $0 \le f \le 1$, accounts for the varying electrostatic effects introduced by the dipole layer at the surface. The sum of $\Delta E_{initial}$ and ΔE_{final} is often found to be close to - 1.1 eV [Er85]. As a further influence, the

---

[15] Nobel price for economics (!) in 1975 (with Leonid Kantorovich).

reduced lifetime of the adsorbed ion as compared to the gas phase ion leads to a peak broadening which usually obscures the vibrational fine structure.

For UV photoelectron spectroscopy, photon energies between 10 and 100 eV are employed. In this energy range, the electrons are emitted from valence orbitals, which participate in chemical bonds and are responsible for the chemical reactivity of the material. This method is especially suitable for surface investigations, since the photoelectrons possess, due to the small mean free path in this energy range, a penetration depth of only a few atomic layers [So81]. Thus, UPS is inherently surface sensitive.

Experimentally, we employed a constant photon energy, $h\nu$, and measured the intensity of the photoelectrons, I_{pe}, as a function of their kinetic energy. The resulting energy distribution curve, $I_{pe}(E_{kin})$, reflects the joint electronic density of states (JDOS), i.e., a superposition of the densities of initial and final states. I_{pe} is proportional to the transition probability, P_{tr}, which is given by Fermi's golden rule:

$$I_{pe} \propto P_{tr} \propto \left| \mu_{fi} \right|^2 \delta\left(E_f - E_i - h\nu\right) \qquad , \qquad \text{(Eq. 4.39)}$$

in which the delta function represents the energy conservation, whereas the transition matrix element

$$\mu_{fi} = \left\langle \psi_f \left| \vec{A}\cdot\vec{p} + \vec{p}\cdot\vec{A} \right| \psi_i \right\rangle \qquad \text{(Eq. 4.40)}$$

guaranties the conservation of momentum.

In the last equations, ψ and E denote the wave functions and energies of the inital (i) and final (f) state, respectively. $\vec{A}$ is the vector potential of the incident light, and $\vec{p}$ is an operator representing the momentum of the photoemitted electron. The orientation of orbitals and, thereby, of adsorbed molecules can be determined on the basis of Eq. 4.40, since variation of the relative orientation of $\vec{A}$ and ψ_i influences μ_{fi} (see Section 4.2.2). During photoemission on solids, the component of the wave vector (and of the momentum) of the electron which is parallel to the surface, $\vec{k}_\parallel$, is conserved (apart from an undetermined contribution of a reciprocal lattice vector). Thus, the measured kinetic energy, E_{kin}, and the electron emission angle θ allow to calculate $|\vec{k}_\parallel|$:

$$|\vec{k}_\parallel| = \frac{\sin\theta}{\hbar}\left(2m_e E_{kin}\right)^{\frac{1}{2}} \qquad \text{(Eq. 4.41)}$$

4.2.2. Experimental aspects

(AR)UPS experiments were performed in the laboratory and, alternatively, at the synchrotron radiation source BESSY-I using a beamline with the toroidal grating monochromator TGM 2 as specified in Ref. [Re95]. The UHV chamber at that beamline was equipped with a commercial electron spectrometer (ADES 400, Vacuum Generators) based on a hemispherical 127° analyzer for electron detection. Details of the analyzer properties can be found in Baalmann's thesis [Ba84]. In the laboratory, the UP spectra were measured with a He discharge resonance lamp providing He-I radiation ($h\nu = 21.22$ eV) and a rotatable 160° spherical sector electron analyzer (Comstock). The photoelectrons were detected normal to the surface ($\phi = 0°$, see Fig. 4.14) if not differently indicated.
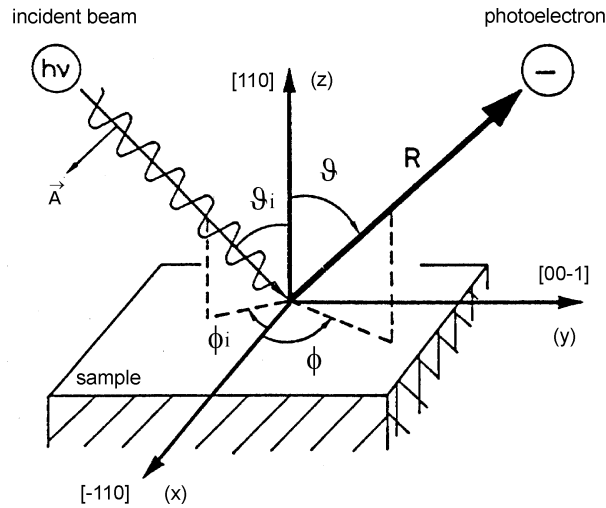

Fig. 4.14: Geometric parameters of our (AR)UPS experiment. Polar (ϑ_i) and azimuthal (ϕ_i) angles of the incident beam. The direction of the ejected electrons is characterized by ϑ and ϕ. Crystallographic planes as indicated. ϕ_i was fixed to 0°, and $\vec{A}$ was parallel to the ($00\bar{1}$) plane.

If the relative intensities of the photoemission signals vary with the incidence angle of the linearly polarized synchrotron UV light, then the dipole selection rules provide additional information about the symmetry of the initial states ψ_i. Depending on the incidence angle we distinguish X, Y, Z, and M ('mixed') polarization, according to the crystal axis which is (approximately) parallel to the vector potential, $\vec{A}$, of the incident wave. As an experimental restriction, the projection of the beam onto the surface was always parallel to the [$\bar{1}10$] (x) direction, i.e., to the trenches of the reconstructed (110) surface, and $\vec{A}$ was parallel to the plane given by surface normal and incident beam (xz or ($00\bar{1}$) plane in Fig. 4.14). Thus, our setup was fixed to p (= 'parallel') polarization. This means, only even inital states (symmetric with respect to the ($00\bar{1}$) mirror plane) could be exited with

synchrotron radiation. (Or, more precisely, only even inital states could be *detected* in normal emission.) Table 4.3 shows the incidence angles for the different polarizations according to the notation used in Fig. 4.12.

During the temperature-dependent UP and $\Delta\varphi$ measurements, the current for the direct sample heating was switched off in order to avoid perturbations caused by the influence of the magnetic field and the electric potential.

polarization	ϕ_i	ϑ_i
X	0°	→ 0° (here 21°)
Y	90°	→ 0° (not used)
Z	0°	→ 90° (here 70° ... 75°)
M	0°	45°

Table 4.3: Incidence angles for UP measurements with linearly polarized sychrotron light. Y polarization could not be used, because, in our experimental setup, $\vec{A}$ had no component in $[00\bar{1}]$ (y) direction.

4.3. Work function measurements

4.3.1. Definition and origin of the work function

From a thermodynamical point of view, the work function of a metal is defined as the minimum energy required for removing one electron from this metal. For the energy to be a minimum, the removed electron must have zero kinetic energy. Then, the work function still depends on the electron's final position, which we may choose at infinitely large distance from the surface. Unfortunately, for a *finite* crystal and the electron at rest in the infinity, different crystal faces should possess the same work function, which contradicts experimental observation. For a *practical* definition of the work function of a finite single-crystal surface, the distance between electron and surface in the final state should be large enough that the image force is negligible (> 1 μm), but small compared to the distance from another face with a different work function. In the case of an adsorbate-covered surface, the final electron-surface distance must also exceed the distance between the adsorbed particles.

Interested especially in surface phenomena, we may split the total work function, φ, into a surface-dependent part, φ_{surf} , and another part, which depends exclusively on bulk properties, $\varphi_{bulk} = \varphi - \varphi_{surf}$. For explaining the origin of φ_{surf} , we adopt a microscopic point of view. The asymmetric forces in the surface region lead to a spill-out of the electron gas and, thereby, to an asymmetric charge distribution or 'dipole layer' on the surface. This surface dipole layer makes the electrostatic potential outside the metal, χ_{∞}, larger than the mean electrostatic potential inside the cystal, $\chi_{-\infty}$, i.e.,

$$\varphi_{surf} = \chi_{\infty} - \chi_{-\infty} \quad . \tag{Eq. 4.42}$$

With the thermodynamical definition given above, the total work function is

$$\varphi = \chi_{\infty} + \frac{E_{N-1}}{e_0} - \frac{E_N}{e_0} \quad . \tag{Eq. 4.43}$$

E_N denotes the initial ground state energy of the neutral crystal and E_{N-1} the energy of the final state with one electron removed. For $T > 0$, the energy difference $E_N - E_{N-1}$ has to be replaced by the electrochemical potential, μ, of the electrons, which can be identified with the Fermi energy E_F:

$$E_N - E_{N-1} \quad \rightarrow \quad \left(\frac{\partial F}{\partial N} \right)_{T,V} \equiv \mu = E_F . \tag{Eq. 4.44}$$

Combining Eqs. 4.42-4.44 we obtain:

$$\varphi = \varphi_{surf} - \frac{\mu}{e_0} + \chi_{-\infty} = \varphi_{surf} - \frac{\bar{\mu}}{e_0} \quad , \tag{Eq. 4.45}$$

with the bulk chemical potential $\bar{\mu} = \mu - e_0 \chi_{-\infty}$. The latter is obviously responsible for the bulk contribution to the total work function: $\varphi_{bulk} = \bar{\mu}/e_0$.

The meaning of these quantities is clarified by Fig. 4.15. For a detailed discussion, see Ref. [Hö79].

A correlation exists between the work function of a metal and its (Mulliken) electronegativity, ξ [Go56]:

$$\frac{\varphi}{[eV]} = 0.72 \frac{\xi}{[eV]} + 0.34 . \tag{Eq. 4.46}$$

The Mulliken electronegativity, χ_M, is given by:

$$\chi_M = \frac{1}{2}(IP + EA) \tag{Eq. 4.47}$$

as the average of the ionization potential, IP, and the electron affinity, EA, of the free atom [Mu34, Mu35].
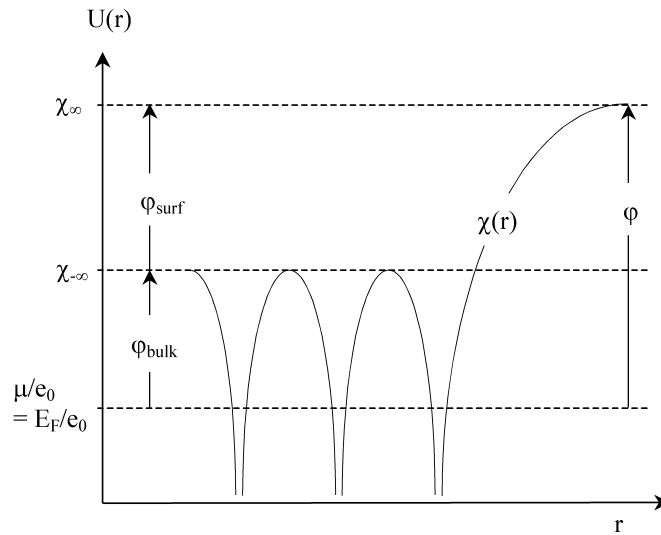
Fig. 4.15: Schematic representation of the electrostatic potential, $\chi(r)$, near a metal surface, together with the other potentials relevant for the definition of the work function (after [Hö79]).
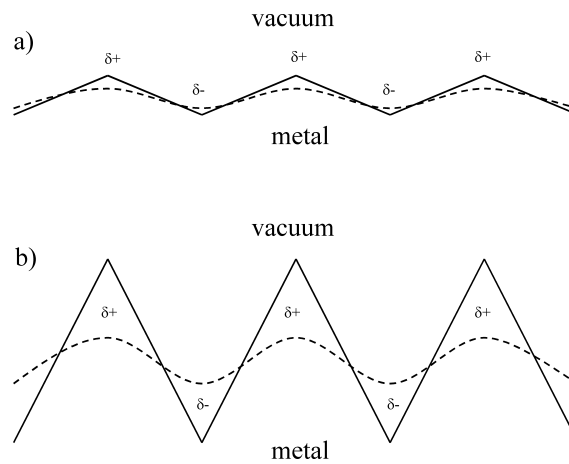
Fig. 4.16: Smoluchowski's corrugated uniform-background model for explaining the different work functions of (a) smooth, closely packed and (b) corrugated, loosely packed surfaces.

4.3.2. Anisotropy of the work function

As a rule, the work function of a loosely packed single crystal surface (as, e.g., Au(110)-(1×2)) is smaller than that of its closely packed counterpart (e.g., Au(111)). This effect has been qualitatively explained by Smoluchowski [Sm41]. He employed a uniform-background model, in which the ion charge is spread over a Wigner-Seitz cell. The metal-vacuum boundary of this uniform-background charge is more or less corrugated, depending on the surface structure (Fig. 4.16, solid lines). It turns out that the contours of the electron density (dashed lines) are considerably smoother than the background boundary.

The resulting charge separation leads to a contribution to the surface dipole moment that has the reverse orientation of the moment due to the electron spill-out. This contribution is smaller for the closely packed surface (Fig. 4.16), and, thus, the surface dipole moment of this surface is larger. This result is in agreement with the experimentally observed higher work function of closely packed, smooth surfaces.

4.3.3. Adsorbate-induced work function changes

According to Langmuir [La32], the charge separation between the adsorbed (especially chemisorbed) particle and the surface leads to a contribution to the dipole moment perpendicular to the surface, which interferes with the spill-out dipole layer of the clean metal surface. The resulting work function change, $\Delta\varphi$, (which equals the change of the surface potential, $\Delta\varphi_{surf}$) is given by the Helmholtz equation:

$$\Delta\varphi = \frac{\mu_0\sigma}{\varepsilon_0} \ .$$ (Eq. 4.48)

If we assume that the dipole moment μ_0 of the adsorbate-substrate complex is independent of the surface concentration (or absolute coverage) σ, we should experimentally find $\Delta\varphi \propto \sigma$, in contradiction to the experimental observation. The usual deviation from linearity is attributed to a mutual depolarization of assumed point dipoles by the Coulomb field of all other point dipoles. According to the frequently used Topping model [To27], the work function change is then given by:

$$\Delta\varphi = \frac{\sigma\mu_0}{\varepsilon_0\,(1+9\alpha\sigma^{3/2})} \quad ,$$ (Eq. 4.49)

in which α stands for the polarizability of the adsorbate-substrate complex.

We only mention that, apart from this classical approach, a quantum-mechanical model has been developed which goes back to Gurney [Gu35].

The interpretation of the work function as electronegativity (vide supra) should allow qualitative considerations about the chemical behaviour of a chemically reactive adsorbate, especially in coadsorption experiments as, e.g., $H_2O/O/Au$.

4.3.4. Experimental determination of the work function and its changes

We may distinguish between two groups of experimental methods for work function measurements: absolute, providing φ, and relative, providing $\Delta\varphi$. Methods of the first group employ electron emission from the sample induced by photon absorption (photoemission) [Si58], by high temperature (thermionic emission), or due to an electric field (field emission) [Go61]. All relative methods (the second group) make use of the contact potential difference between the sample and a reference electrode. The work function of the reference electrode is often unknown, making the determination of absolute values impossible. Experimentally, either the anode current of a diode is used (diode methods), or the displacement current between the electrodes (sample/reference), created by an artificial change in the capacitance between the two electrodes, is measured (condenser methods). A widely used condenser method is the vibrating capacitor method, named after William Thomson [Th89], the later Lord Kelvin. In the following, we confine ourself to describing the photoemission method in the way we employed it extensively in this work.

THE PHOTOEMISSION METHOD – For measuring *absolute* work function values (which is advantageous because it allows to assess the cleanliness of the surface), we made use of the fact that the width of an UV-photoelectron spectrum is a measure for the work function.

The kinetic energy of a photoelectron, $E_{kin}(s)$, emitted from a solid with the work function φ_s amounts to:

$$E_{kin}(s) = h\nu - E_b - e_0\varphi_s \quad , \tag{Eq. 4.50}$$

whereas the *measured* kinetic energy, $E_{kin}(sp)$, depends on the work function of the spectrometer, φ_{sp}:

$$E_{kin}(sp) = h\nu - E_b - e_0\varphi_s \quad . \tag{Eq. 4.51}$$

(For the meaning of the other symbols see Section 4.2.)

Electrons emitted from the Fermi level ($E_b = 0$) possess the maximum kinetic energy, i.e., the onset of emission in the measured spectrum occurs at:

$$\max E_{kin}(sp) = h\nu - e_0\varphi_{sp} \; .$$

(Eq. 4.52)

The smallest possible kinetic energy is $\min E_{kin}(s) = 0$, and therefore

$$\min E_{kin}(sp) = e_0\varphi_s - e_0\varphi_{sp} \; .$$

(Eq. 4.53)

If $\varphi_{sp} < \varphi_s$, then φ_s can easily be determined from the width of the UP spectrum, ΔE, i.e., from the difference between Fermi level and secondary electron cutoff edge:

$$\Delta E \equiv \left\{ \max E_{kin}(sp) - \min E_{kin}(sp) \right\} = h\nu - e_0\varphi \; .$$

(Eq. 4.54)

Since we know $h\nu$ with high accuracy, especially when using radiation generated by a gas discharge, we can measure precise absolute work function values. For a less precisely known photon energy, as in the case of synchrotron radiation, we can still measure accurate work function changes.

A problem arises in the case of $\varphi_{sp} > \varphi_s$, as illustrated in Fig. 4.17. Photoelectrons with $E_{kin}(s) < e_0\varphi_{sp} - e_0\varphi_s$ are not able to surmount the contact potential difference between sample and spectrometer. As a consequence, ΔE is a measure for φ_{sp}, rather than for φ_s.

In order to avoid this problem, we applied a negative potential (-10 V) to the crystal during the measurements, which ensures $E_{kin}(s) > \varphi_{sp} - \varphi_s$. As further advantages, the negative bias voltage on the sample reduces the influence of low-energy electrons from other sources (e.g., ionization gauge) and separates the UP spectrum from secondary electrons produced in the spectrometer. With the position of the Fermi level fixed in this way, any change in the width of the spectrum leads to a a shift of the cutoff edge on the energy scale. The position of the cutoff edge was measured at 50% of the maximum photoelectron intensity, which approximately coincided with the point of inflection.

In adsorption/desorption experiments, we determined work function changes, $\Delta\varphi$, by a *continuous* measurement of the width of the corresponding UP spectra. Controll of the experiment and data aquisition was achieved by a personal computer (PC). The energy analyser was controlled by a DA converter; and the corresponding photoelectron intensity was fed into an AD converter (both Computer Boards, Inc.) after conversion of the pulse rate into a voltage, performed with a rate meter. A computer program first determined the inital position of the secondary electron cutoff edge and calculated the initial work function value. Any work function change, e.g. due to adsorption, shifted the cutoff edge

and led to a change in the photoelectron intensity at the initial energy position. As the next step, the program varied the analyser energy until the initial intensity was regained. The value of this energy shift equals the work function change and was recorded. A further work function change was again compensated by another variation of the analyser energy, and so on. Typically, 10 - 20 controll loops per second were performed. This method has been developed, refined, and in detail described by K.J. Schmidt [Sc02].

Limiting to the accuracy is the noise generated by the control loops. Still, the accuracy of the $\Delta\varphi$ measurement was better than 10 meV. The *absolute* work function values have an error < 50 meV.
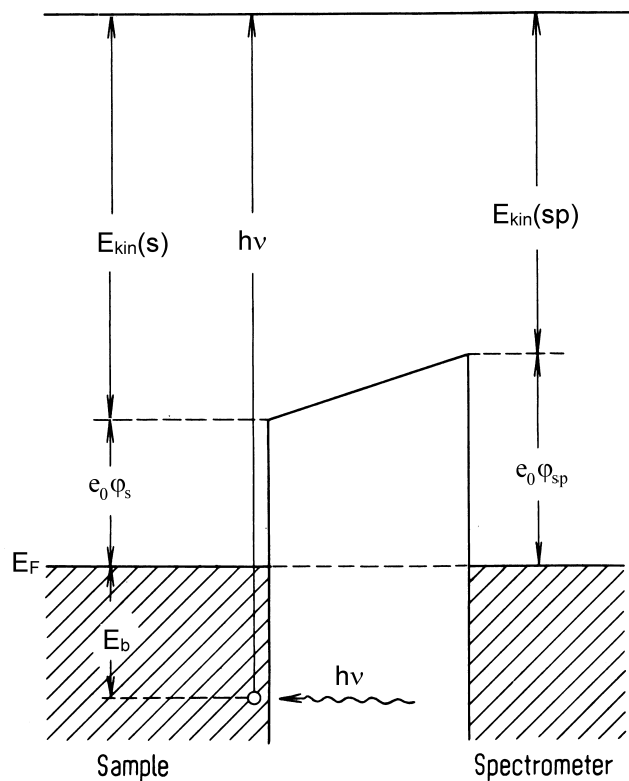
$$E_{kin}(s) \quad h\nu \qquad\qquad E_{kin}(sp)$$

$$e_0\varphi_s \qquad\qquad\qquad e_0\varphi_{sp}$$

$$E_F$$

$$E_b$$

$$h\nu$$

Sample   Spectrometer

Fig. 4.17: Energy level diagram for excitation and detection of photoelectrons. For the case $\varphi_{sp} > \varphi_s$, which is here displayed, photoelectrons with $E_{kin}(s) < e_0\varphi_{sp} - e_0\varphi_s$ cannot reach the spectrometer.

4.4. Low-energy electron diffraction (LEED)

Low energy electron diffraction, as an effect discovered by Davisson[16] and Germer in 1927 [Da27] and developed as a surface science tool by Germer et al. around 1960 [Sc60], is presently the most important technique for investigating periodic structures on electrically conducting surfaces which can resist the electron impact. The applied electron energies, typically between 10 eV and 500 eV, fall within the range of the minimum in the universal inelastic mean free path curve of electrons in solids, which makes LEED inherently surface sensitive. As a basic application, LEED is employed for determining the symmetry of the surface unit cell and for a qualitative assessement of the long-range order by examining shape and sharpness of the diffraction reflexes. This is the level on which LEED is applied throughout this work. For explaining those diffraction patterns, only single scattering of the electrons has to be considered – this is field of the kinematic LEED theory, which is very similar to the theory of x-ray diffraction. However, the large cross section for elastic electron scattering ($\approx 1\text{Å}^2$, comparable to the inelastic scattering cross section) causes a high probability for multiple scattering. A complete ('dynamical') LEED analysis, which allows to determine atomic positions in the unit cell, has to consider the complicated multi-scattering electron trajectories and is therefore a difficult procedure that involves hugh computational effort [Pe74].

In this work, we applied a commercial four-grid LEED optics (Varian). For image recording, we used a CCD camera. A schematic sketch of our LEED system can be found in Ref. [Go99].

4.5. Near edge x-ray absorption fine structure (NEXAFS) spectroscopy

The fine structure above the x-ray absorption edge of a core level can be separated into a *n*ear-*e*dge region (NEXAFS) [St92], which is located within ≈ 30 eV above the edge, and an *e*xtended region at higher photon energies (EXAFS) [Ha85, Ha92]. Due to the small inelastic mean free path of the photoelectrons in the respective energy range, NEXAFS is dominated by multiple scattering, in contrast to EXAFS. Therefore, the NEXAFS theory is complicated, for which reason NEXAFS is mostly used to determine molecular orientations by observing the polarization dependence of the resonance intensity, which is mainly controlled by well-established symmetry selection rules (see below). (EXAFS, on the other hand, provides much more information e.g. about bond lengths and local geometries of adsorption sites.)

The signals in the NEXAFS region can be divided into σ and π resonances. The lower energy π resonances are assigned to transitions from the core level into an unoccupied molecular orbital of (local) π symmetry. Thus, the NEXAFS spectroscopy probes (partially) empty levels below the ionization theshold just as inverse photoemission does.

---

[16] Nobel price 1937 (with G.P. Thomson).

The σ resonances, which occur at higher energies, are associated with final-state scattering resonances (or shape resonances). They are believed to correspond to quasi-bound states in the continuum above the vacuum level in which certain angular momentum components of the photoelectron wave are resonantly trapped by a potential barrier. The latter arises from centrifugal forces which result in a concentric double well potential. Alternatively, both resonances can be explained by a MO picture, in which the σ resonances are assigned to transitions into antibonding σ* molecular orbitals in the continuum. From these interpretations, which are essentially equivalent, the latter is certainly more appealing to the chemist. It should be mentioned that more recent works cast doubts on the existence of shape resonances [Ke97].

The photon absorption is controlled by dipole selection rules, which lead to the following general relations for the angle-dependence of the resonance intensities I [St81]:

$$I_\sigma \propto \cos^2 \beta \qquad \text{(Eq. 4.55a)}$$

$$I_\pi \propto \cos^2 \gamma \qquad \text{(Eq. 4.55b)}$$

In these equations, β and γ are the angles between the polarization vector and the bond axis (β) and the direction perpendicular to this axis (γ). Making use of the polarized nature of the synchrotron radiation we can therefore determine the orientation of the adsorbed molecule relative to the surface.

We performed our NEXAFS experiments at BESSY-II, beamline PM 1 during a single two-weeks session within the test phase of the synchroton. Regular beam time was only sporadically available. The spectra were recorded with a channel plate detector by partial-yield detection with a retarding voltage of -140 V. The raw spectra were divided by the signal of the clean surface as a correction for the monochromator transmission function and the background signal. Alternatively, division by the electron yield signal from a reference gold grid monitor, measured concurrently with the sample, led to practically identical results. This procedure was not employed here due to the higher noise level in the resulting spectra.

4.6. Sample preparation and UHV system

THE SAMPLE consisted of a cylindrical Au single crystal (∅ 10mm) with a polished (110)-(1×2) surface, mounted with Ta wires (∅ 0.25mm) to a Mo sample holder. The Ta wires also allowed resistive heating of the crystal. The sample could be cooled to 28 K by means of a commercial He cryogenerator (Leybold RGD210) with an electrically isolated Mo rod establishing the thermal contact to the sample holder. A detailed description of the cryo-system can be found in Refs. [Re96] and [Sc02]. The sample temperature was monitored by means of a chromel-alumel thermocouple pressed into a hole on the crystal

edge. For more details about the temperature measurement, see Section 4.1.2. The (110)-(1×2) surface of the crystal was cleaned by repeated cycles of Ne ion sputtering and annealing at 650 K until an AES-clean surface with the 1×2 LEED pattern characteristic of the reconstructed Au(110) surface was obtained. Further confirmation of the absence of certain contaminants (Ca, Si, and Mg) were the inertness of the sample towards molecular oxygen and the absence of extra features in the TD spectra of physisorbed gases like O_2, CO, or Kr.

THE APPARATUS - The experiments were performed in a stainless steel ultra-high vacuum chamber with a combined ion getter and turbomolecular pumping system providing a base pressure of 5×10^{-11} mbar. The chamber was equipped with a mass spectrometer (Balzers QMS 511, later QMS 112), a four-grid LEED optics (Varian), an electron gun (Varian) for AES and an ion gun (Leybold) for sample preparation and oxygen ion bombardment. A complete description of the vacuum system was given by Schmidt [Sc02]. For (AR)UPS experiments, a gas discharge resonance lamp and a rotatable 160° spherical sector electron analyzer (Comstock) were employed (see Section 4.2). The electron bombardment experiments were carried out using an electron gun with a large angle of emission (flood gun, Leybold). Many of the (AR)UPS and all UV activation experiments were performed at the synchrotron radiation source BESSY-I using a beamline containing the toroidal grating monochromator TGM 2. The vacuum chamber connected to that beamline was equipped with a commercial electron spectrometer (ADES 400, Vacuum Generators) containing a hemispherical 127° electron analyser. Furthermore, facilities for TDS, AES, and LEED and an ion source were available.

The NEXAFS experiments were performed at the synchrotron radiation source BESSY-II using a beamline equipped with the plane grating monochromator PM 1. Further experimental details can be found in Section 4.5.

Residual gas analysis and (reactive) thermal desorption measurements were performed by means of a differentially turbo-pumped mass spectrometer mounted in a cone with a small orifice. Experimental details about the TDS measurements are given in Section 4.1.

Work functions were measured with an accuracy of ±10 meV by monitoring the low-energy cut-off edge of UV photoelectron spectra (see Section 4.3).

Gas exposures were performed by backfilling of the vacuum chamber using leak valves. For the pressure measurements, which have an error of 20 %, we employed a Bayard-Alpert type ionization gauge. The different gauge sensitivities for the particular gases were compensated by dividing the meter reading by the following factors: O_2 0.8, CO 1.1, CO_2 1.45, C_2H_4 2.14, Kr 1.86.